Corrosion Science (2010) 52:7, 2469-2480

On the penetration of corrosion products from reinforcing steel into concrete due to chloride-induced corrosion

H.S. Wong[a *], Y.X. Zhao[b], A.R. Karimi[a], N.R. Buenfeld[a] and W.L. Jin[b]

[a] *Concrete Durability Group, Imperial College London, SW7 2AZ, UK*

b College of Civil Engineering & Architecture. Zhejiang University. Hangzhou 310027. P. R. China

Abstract

Reinforced concretes were corroded to varying degrees by exposing to cyclic NaCl spray and 40˚C drying. The amount of corrosion products and induced damage were measured using image analysis. We found that corrosion products can accumulate at steel-concrete interface as well as penetrate cement paste and deposit within hydration products, relicts of reacted slag, and air voids. As corrosion increases, the products tend to accumulate at the steel-concrete interface, while the amount penetrating cement paste remains relatively constant. Only a small amount of corrosion is needed to induce visible cover cracking. Implications on modelling time to cover cracking are discussed.

Keywords: Steel reinforced concrete (A); SEM (B); Modelling studies (B); Interfaces (C); Rust (C)

1. Introduction

Corrosion of steel in reinforced concrete is an electrochemical process that causes the dissolution of iron to form a range of solid products. Corrosion products is a complex mixture of iron oxides, hydroxides and hydrated oxides that evolves according to the prevailing local environment [1, 2, 3]. Depending on their level of oxidation and the availability of moisture, corrosion products have specific volumes ranging from about two to six times that of the iron consumed [4, 5]. As such, the main damage caused by corrosion of reinforcement in concrete is not the loss of steel cross section, but cracking of the concrete cover due to expansive stresses exerted by the continued deposition of corrosion products near the steel-concrete interface. This leads to progressive deterioration and even spalling of the cover.

However, not all corrosion products contribute to the build-up of stresses and initial cracking of the cover. Despite the apparent insolubility of the final corrosion products, the process of corrosion involves soluble species that can dissolve in the concrete pore solution and subsequently migrate or diffuse through the cement paste matrix away from the corroding steel [6, 7]. In the presence of chloride ions, the dissolution of iron is increased by formation of intermediary chlorocomplexes, i.e. ‘green-rusts’ [9]. These soluble complexes migrate away from the anodic sites, and subsequently break down in oxygen-rich areas, releasing the chlorides to transport more ferrous ions from the corroding steel [4, 8, 9]. The mobility of these soluble species and subsequent precipitation in oxygen-rich areas results in the corrosion products being distributed within the porous cement paste.

The ability of the pore structure (capillaries, microcracks and air voids) to accommodate corrosion products, at least in the initial stages of corrosion, may have an effect of prolonging the time to cracking of the concrete cover. The pores

* Corresponding author: H.S. Wong; Email: hong.wong@imperial.ac.uk; 228B Skempton Building, Imperial College London, SW7 2AZ UK, Phone: +44 2075945956; Fax: +44 2075945989

near the corroding steel act as repositories, hence extending the period between onset of corrosion and pressure development that leads to damage of the concrete cover. This effect has been shown experimentally for example, by using hydraulic pressurisation to simulate the corrosion and damage processes in reinforced concrete [10]. Alonso et al [11] observed that an increase in porosity (w/c ratio) produces a delay in crack initiation and this was attributed to the higher amount of void space available to accommodate corrosion products without stress generation. Indeed, many recent theoretical models for predicting time to initial cover cracking have incorporated a 'free-expansion' step to account for the time needed for corrosion products to fill the porous cement paste around the rebar. For example, Liu & Weyers [12] assumed the existence of a 12.5μm thick 'porous zone' around the steel that must be filled with corrosion products prior to any development of expansive pressure. This has been adopted in many subsequent works by others (e.g. [13, 14]) although without any experimental verification. In another study [15], a 40 μm thick 'porous zone' with the porosity estimated using Powers' model was proposed instead.

Very little previous research has examined the amount and distribution of corrosion products and their effect on the microstructure of the steel-concrete interface and contribution to cover cracking. Previous studies, using various analytical and microscopy techniques, have shown that corrosion products forms in the cement paste adjacent to a corroding rebar [e.g. 7, 16, 17, 18, 19, 20, 21, 22], Various studies of corrosion in archaeological artefacts containing metallic reinforcements found that the steel-binder interface contains a dense inner corrosion product layer and a transformed medium that contains corrosion products and elements from the binder [23, 24]. However, there have been no rigorous attempts to quantify the extent and distribution of the corrosion products accumulation at the steel-concrete interface and penetration into the adjacent cement paste, and their damaging effects. Presumably, the amount of corrosion products that can be accommodated during free expansion depends on the volume and connectivity of the pore structure, which is in turn related to factors such as mix composition, degree of hydration and compaction. Thus, assuming a constant value for all cases in modelling appears to be an oversimplification, but a more refined approach is not currently possible since fundamental understanding of this phenomenon is lacking. Clearly, research is needed in this area in order to advance service-life prediction models based on estimating time to cover cracking.

The objective of this work is to characterise the amount and distribution of corrosion products, particularly during the transition period between corrosion initiation and the development of significant damage. Our study is based on reinforced concrete samples that have been subjected to salt spray on one exposed surface to induce corrosion and cover cracking. It was decided that corrosion should not be accelerated by admixed chlorides, imposed electrical current or manufactured cracks, because such treatments would artificially influence the formation and distribution of the corrosion products. The samples examined should span a range of degrees of corrosion; however, severely deteriorated samples are excluded because their microstructure would have been significantly altered since the time of crack initiation. To obtain objective and quantitative information, measurements should be made on many flat, random cross-sections of the corroded rebar-concrete interface, but sample preparation can be challenging and problematic. Irregular, fractured surfaces, although easier to study, are not representative because these tend to expose more of the damaged and corroded areas. Fractured surfaces also do not allow accurate measurements to be made.

2. Experimental

2.1 Materials

The samples examined were taken from reinforced concrete panels that contained three 16mm nominal diameter deformed (corrugated) carbon steel bars at 20 mm cover spacing (Fig. 1). The steel had a composition of C: 0.14-0.22%, Si: 0.12-0.30%, Mn: 0.30-0.65%, P < 0.045% and S < 0.050%. The rebars were used as-received and no efforts were made to remove existing millscale. More than one thousand panels were prepared as part of a long-term research project on chloride-induced corrosion in a cyclic wet/dry environment. The low cover depth of 20 mm was adopted to reduce the time to corrosion initiation. Some of the panels were made from 'high-performance concrete' (HPC), cast in situ by a construction company in accordance with specifications used for reinforced concrete elements of a major sea crossing in China. The other panels were made from 'normal concrete' (NC), cast in the laboratory for comparison.

The mixture proportions are shown in Table 1. Mix NC was an ordinary Portland cement concrete while mix HPC was a triple blended concrete that contained slag and fly ash at 40% and 30% replacement levels respectively. The water/binder ratios were 0.44 and 0.345 for NC and HPC respectively. The cement used was a Portland cement that conforms to CEM 1 42.5N (EN197-1:2000). The cement had a chloride content of 0.06%, sulphate content of 3.5% and loss on ignition of 3%. The HPC contained a commercial calcium nitrite based corrosion inhibitor. The gravel and sand were siliceous aggregates at 20 mm and 5 mm maximum size respectively. The 28-day compressive strengths of NC and HPC, as measured on 150 mm cubes, were 50 MPa and 56 MPa respectively. The chloride diffusion coefficient calculated from acid-soluble chloride profile for NC was of the order 10^{-11} m^2/s (at 12 months). The chloride diffusion coefficient for HPC was of the order 10^{-12} m^2/s (at 3 months). Acid-soluble chlorides were extracted from powdered samples at 0.5 mm depth increments from the surface and the chloride content (% concrete mass) was measured using a calibrated electrode by Germann Instruments A/S. A chloride profile was then fitted to the measured results using the error function solution of Fick's second law of diffusion to calculate the apparent diffusion coefficient.

2.2 Curing and exposure to chlorides

Immediately after casting, the panels were covered with damp hessian and sprayed with water once a day for 14 days, after which, they were allowed to dry at room temperature (~25°C) for several weeks. The side and bottom surfaces of each panel were then surface treated with epoxy resin and a polyurethane coating to ensure that chloride predominantly penetrated through the top cover, with minimal penetration through the other faces of the panel. This approximates to the condition of slabs and walls, e.g. bridge decks and car park floors, where chloride transport is unidirectional. The panels were then placed in an environmental chamber and subjected to cyclic wetting and drying to induce corrosion. Each wet/dry cycle lasted for 3 days and consisted of spraying with 3.53% wt. NaCl solution for 4 hours and subsequent drying at 40˚C for the remaining period. After about 12 months of exposure, a small number of the panels were affected by corrosion. Fine longitudinal cracks were observed on the top face, running approximately parallel to the reinforcing bar. The widths of the visible cracks varied along the length of the affected panels. Brownish-red rust stains were seen on the external side surfaces of some panels. However, the front and bottom faces showed no signs of cracking. Two panels, one from each mix, were subsequently removed from the environmental chamber for further testing. These had longitudinal cracks that covered about 40% and 20% of the length of the NC and HPC panels respectively. The widths of the cracks measured on the surface ranged from 0.05 to 0.9 mm.

2.3 Sample preparation for imaging

The two selected panels were carefully cut with a diamond saw to extract the corner and middle rebars, with their surrounding concrete intact. Sectioning was done at least 15 mm away from the rebar to minimise any disturbance to the rebar-concrete interface. The sectioned panels were labelled NC-A, NC-B and HPC-A, where A and B represent the sections containing the corner and middle rebars respectively. The middle rebar of the HPC panel was not further tested since it was unaffected by corrosion. The sectioned panels were then dried at 50˚C, impregnated with a low viscosity epoxy (Struers Epofix), which encapsulated the entire section and filled any cracks connected to the outer surface. The epoxy was allowed to harden for several days. Each section was then cut sequentially starting from the side face to produce a series of 8mm-thick cross-section slices, until no corrosion could be seen at the rebar-concrete interface. An example of a slice is shown in Fig. 2. Cutting was carried out using an automatic abrasive cutter and diamond cut-off blade designed for hard brittle materials, at a very low feed rate (<0.3 mm/s) with water as lubricant. Fifty-seven slices were produced in total and the location of each within the respective panels was marked on each slice. For example, 'NC-A-60' represents a slice from panel NC-A at 60 mm from the side face. Tests using phenolphthalein spray found no signs of carbonation. The slices were immediately dried with paper towel, then dry ground with SiC papers at 500, 1000 and 1200 grit sizes, and cleaned with acetone. The slices were examined immediately and kept in incubators containing soda lime and saturated magnesium chloride (r.h. 35%) to avoid carbonation or further corrosion of the exposed rebar.

2.4 Flatbed scanning

Each ground slice was visually inspected and then imaged using a conventional flatbed scanner (Epson Perfection 2450) at 1200 dpi to produce a colour image (e.g. Fig. 2) that shows the corrosion products at the rebar-concrete interface, cracks, rebar, aggregate, paste and epoxy. The image was enhanced by increasing the level of contrast and colour saturation, then cropped and segmented to produce binary images of the corrosion products, cracks and rebar. In Fig. 3, the original and segmented images of two slices having different degrees of corrosion and cracking are shown. Segmentation was done by zooming into the image and manually tracing the boundaries of the features of interest. This was cross-checked by examining the actual slice specimen with the stereomicroscope (Olympus SZX9). The contrast for the rebar, cracks (>0.1 mm) and corrosion products at the rebar-concrete interface was generally good, thus the accuracy of segmenting these should be satisfactory. Although the presence of corrosion products enhances the visibility of the finer cracks, the smallest detectable crack width was probably only about 0.05 mm. The resolution of the scanned image, however, is insufficient to differentiate the corrosion products that penetrated the cement paste from those that accumulated between the rebar and concrete. The area of the segmented corrosion products was measured for each slice and expressed as a percentage of the original rebar cross-sectional area. Similarly, a degree of damage was estimated from the area fraction of the cracks. Note that the degree of damage does not include the corrosion product area (Fig. 3c). The original rebar areas for NC-A, NC-B and HPC-A were 192.9 ± 1.4 mm^2, 190.8 ± 0.6 mm^2 and 201.2 ± 0.8 mm^2 (mean ± standard error) respectively. These were measured separately and averaged from five different slices that were not affected by corrosion.

2.5 Backscattered electron imaging

A field-emission scanning electron microscope (Camscan Apollo) operated in the backscattered electron (BSE) mode was used to study the microstructure at the steel-concrete interface. The main objective was to find areas where corrosion products had penetrated the cement paste and to carry out measurements to study their size, distribution, and relation to the amount of corrosion and damage. Nine slices that showed a range of degrees of corrosion were selected from NC-A, NC-B and HPC-A. They were vacuum-impregnated with a low viscosity epoxy, trimmed down to a 50 x 25 x 8 mm block, and then ground with SiC papers at 500, 1000 and 1200 grit to expose a fresh surface and polished using diamond with successively finer grit size to a ¼ μm finish. Polishing time at each stage was kept short to minimise surface relief and pull-out defects. An oil-based fluid was used as lubricant and acetone for cleaning. A 5nm thick layer of gold (measured with a film thickness monitor) was sputtered onto the polished surface and silver paint applied on the edges to avoid charging artefacts. Images were captured at 15 kV, using the same brightness and contrast settings to enable comparison between different locations and samples. The orientation of the images is such that the top corresponds to the direction of the exposed cover.

2.6 Energy dispersive X-ray microanalysis

Qualitative and quantitative X-ray microanalysis (EDX) was carried out in the electron microscope, which was fitted with an energy dispersive X-ray spectrometer (Oxford Instruments). An accelerating voltage of 15 kV was chosen as a compromise to achieve a good spatial resolution and low X-ray absorption of the lighter elements, and to provide a sufficient overvoltage for exciting heavier elements such as Fe [25]. The beam current, measured with a Faraday cup, was maintained at 1.5 nA. This provided an acquisition rate of about 3 kcps at 30% dead time, on all points measured. Qualitative element mapping was carried out at 128x104, 256x208 or 512x416 pixel resolution, to approximately match the size of the X-ray generation volume at the current microscope settings, which can be determined via Monte-Carlo simulations [26]. Beam dwell time was set at 100 μs and more than 250 frames were averaged to produce the element maps.

For quantitative spot analyses, X-rays were collected for 100 s at each spot to obtain a total count greater than 300k per spectrum. The locations for spot analyses were not random, but chosen by examining the BSE image. Again, consideration was taken of the relative size of the X-ray generation volume and the feature of interest to avoid sampling more than one phase where possible, however most analyses, particularly in the C-S-H gel, are likely to represent mixtures. To obtain a representative result, a large number of spots (typically > 50) were analysed and averaged. A cobalt standard (MicroAnalysis Consultants) was used to calibrate and monitor beam stability approximately every 2 hours. The beam rarely changed by more than 1% between calibrations. Natural minerals and pure metals were used as reference standards, and matrix corrections were applied using the XPP procedure [27]. Measurements were made for O, Na, Mg, Al, Si, S, Cl, K, Ca, Ti, Mn, Fe, Co and Au. Analysis totals, i.e. the sum of all elements present, were determined in the conventional way by assuming that oxygen is bound by predefined stoichiometry to all the other analysed elements [28, 29, 30].

3. Results

3.1 Visual inspection

Visual inspection of the slices immediately after cutting using a stereomicroscope found that the colour of the corrosion products is mainly dark brownish-red, although in some areas the corrosion products tend to be of a brighter red hue. The slices exhibited various amounts of corrosion and cracking, but it was clear that those taken from near the side face of the panels were more affected than farther away (Fig. 3). In every slice, the corrosion products at the steel-concrete interface are not uniformly distributed around the rebar, but accumulated mainly in the upper half, where it is closest to the untreated top cover as can be seen in Figs. 2 & 3. This suggests that the corrosion of the rebar is spatially variable due to the non-uniform distance to the exposed concrete surface and possibly pitting corrosion.

Most cracks near the steel-concrete interface are completely filled with corrosion products, while cracks farther away are partially filled or have surfaces lined with corrosion products, and the remaining space filled with epoxy from the first impregnation. In all slices that were affected by corrosion, there was at least one major crack that propagated from the rebar through the full depth of the top cover. The average surface crack width at the top cover was 0.35 mm; the smallest and largest crack widths were 0.05 mm and 0.9 mm respectively. Slices that had no visible corrosion did not show any cover cracking.

3.2 Amount of corrosion and induced damage

Fig 4a presents the amount of corrosion and damage measured using the procedure outlined in 2.4. The correlation between corrosion and damage shows that crack propagation and growth is strongly related to the accumulation of corrosion products at the steel-concrete interface. The slices from the corner rebar (NC-A) appear to be slightly more damaged than those from the middle rebar (NC-B), given the same amount of corrosion. Despite some apparent scatter, the data can be fitted by a linear regression line ($y = 1.51x + 0.18$, $r^2 = 0.86$) with an intercept that passes near the origin. However, the image analysis procedure (2.4) cannot distinguish between corrosion products that had penetrated the cement paste and those that did not, thus a more detailed study using BSE microscopy was required.

Fig. 4b plots the variation in corrosion along the length of the panels. The results show that corrosion is more severe on slices taken near the side face compared to those farther away. The results also suggest that corrosion probably initiated near the side face, perhaps due to a failure of the protective side-surface coating as indicated by rust stains observed on the external side surface of the panel. Another possibility is that cracks, induced by corrosion, had caused the side coating to fail. This provided an easy access for chlorides, moisture and oxygen to the rebar, hence accelerating the corrosion near the side face. However, the observation that the corrosion products mainly accumulated on the upper half of the rebar cross section (e.g. Fig. 3) suggests that ingress of chlorides, oxygen and moisture through the top cover also played an important role. Compared to NC, the slices from HPC showed slightly less damage given the same amount of corrosion. However, the length of the rebar affected by corrosion in HPC-A was significantly less; ~50 mm compared to ~120 mm for NPC-A and ~80 mm for NPC-B.

3.3 Microstructure characteristics

Non-corroded interface

In non-corroded areas, the steel is covered by a layer of millscale (Fig. 5a) with thickness ranging from approximately 20 to 50 μm. The millscale has a characteristic fractured appearance throughout. A bond failure is often seen between the millscale and concrete. This is probably sample preparation damage due to differential expansion and shrinkage when the samples were dried. EDX spot analysis (Table 2) found that the millscale contains mainly (>96% wt) Fe and O, with mean Fe/O atomic ratio of 0.91 (± 0.04). This suggests that it is predominantly wustite (FeO) with minor amounts of magnetite (Fe_3O_4) or hematite (Fe_2O_3). These are the expected iron oxides that form at high temperatures [31]. All other elements were trace (<0.5% wt). A sharp contrast is particularly evident in the element maps for Fe, Ca and Al + Mg (Fig. 5b), where Fe is mostly detected in the steel and millscale, while Ca, Al and Mg are found only in the cement paste matrix. The Al + Mg map highlights the slag and fly ash particles that are present in the HPC mix. The distinct separation between the Fe and Ca shows that very little or no migration has occurred in a non-corroded interface.

Corroded interface

Fig. 6 and 7 show BSE montage images obtained from NC-A-110 that had a low level of corrosion (0.98%) and from NC-A-20 and HPC-A-40 that had higher levels of corrosion (6.81% and 6.65% respectively). The montage images were produced by aligning and merging multiple images captured at high magnification so that a larger, more representative field of view is obtained without compromising resolution. In areas of low corrosion (Fig. 6), the millscale is largely intact, but shows signs of deterioration and further oxidation. Some corrosion products can be detected between the millscale and steel. EDX analysis also found higher concentrations of Cl in this area (~3% wt at high points).

In severely corroded areas (Fig. 7), the millscale is completely oxidised and replaced by a thick layer of corrosion products (~600 μm) that has accumulated at the steel-concrete interface. For convenience, this is abbreviated as 'CL' (corrosion-layer) in the BSE images. The corrosion layer does not contain any aggregate or cement paste from the concrete. Remnants of dislocated millscale are sometimes still visible, and this is usually found near the outer edge of the corrosion layer. This suggests that movement of the millscale has occurred due to expansion and growth of the corrosion layer from the reaction zone at the steel boundary.

The corrosion products accumulated at the steel-concrete interface usually appear featureless and uniform, but occasionally a layered structure of dark and lighter bands can be seen. Such layers probably resulted from varying levels of oxidation that is dependent on the prevailing conditions, particularly the availability of oxygen [9]. This is supported by EDX spot analysis (Table 2) that measured a lower mean Fe/O atomic ratio (0.56 ± 0.02) in the darker corrosion band, which suggests formation in an oxygen-rich environment, compared to the lighter band (Fe/O = 0.84 ± 0.08). The darker band also has marginally higher contents of Ca and Na (~1% wt) and lower analysis totals (~89%) compared to the lighter band (<0.5% wt, 93% analysis totals). The presence of these cations and totals less than 100% suggest that the corrosion layer is porous and permeable, as observed in previous studies [9, 23, 32]. The layered structure of the corrosion products has also been observed by others in ancient buildings containing ferrous reinforcements. Using μXRD and μRaman techniques, Chitty et al. [23] showed that the corrosion product layer is constituted of a matrix of iron oxy-hydroxides (goethite α-FeOOH, akageneite β-FeOOH, lepidocrocite γ-FeOOH) that contains marblings of iron oxides such as maghemite (γ-Fe_2O_3) and/or magnetite (Fe_3O_4).

Cement paste

From the BSE images in Fig. 6 and 7, it can be seen that some parts of the cement paste adjacent to the corroding steel are brighter than the cement paste farther away. This suggests an increase in the local mean atomic number and backscattering coefficient, perhaps due to ingress of a heavy element (e.g. Fe) into the paste. This is confirmed by the EDX element maps in Fig. 6, which show high concentrations of Fe in the steel and millscale, and significant levels extending into the paste. The amount of Fe detected in the paste is far more than that expected from the unreacted cement (see Fig. 5b). A high level of O is also found in this region. The paste area that contains high Fe and O matches very well with the area that is brighter in the BSE image. Interestingly, the Ca map indicates that some leaching or decalcification has also occurred in the affected areas. The affected paste is abbreviated as 'CP' (corrosion-penetrated paste) in the BSE image.

Comparing Fig. 7 to Fig. 6, it appears that a more extensive penetration of corrosion products has occurred in samples that had higher levels of corrosion. However, the depth of penetration does not appear to have increased significantly, indeed many locations showed little or no visible penetration despite significant build up of corrosion products at the steel-concrete interface (e.g. Fig. 7b, Fig. 8). Interestingly, there does not appear to be any preferential location within the cement paste where the corrosion product migrates; it accumulates at the aggregate-paste 'interfacial transition zone' (as previously observed by Gallias [33] and Aligizaki et al [18]), as well as in the 'bulk' paste farther away. This despite the fact that the interfacial transition zone (ITZ) is known to contain on average, higher porosity than the bulk paste due to inefficient particle-packing and bleeding effects. No appreciable amounts of Fe were detected within the aggregate particles, presumably because they are of low porosity compared to the cement paste. In fact, in many locations, the aggregates appear to impede the movement of corrosion products.

Air voids and cracks

The HPC sample had visibly more entrapped air voids than the NC samples. This suggests poorer compaction of the HPC, perhaps attributable to its lower w/c ratio. Many air voids can be seen in the vicinity of the rebar-concrete interface. Those located near the corroding zone (<500 μm away) tend to be filled with corrosion products (e.g. Fig. 7b) and their surrounding cement paste also contains higher concentrations of Fe and O. Many of these air voids do not appear to be in direct contact with the corroding steel.

In every corroded sample, macrocracks with widths greater than 50 μm can be seen propagating from the corroding steel (e.g. Figs. 7 & 8) through the full thickness of the top cover. These macrocracks are caused by expansive stresses exerted by the corrosion products at the rebar-concrete interface. It is noted that some cracks are partially filled with corrosion products while others remain empty. In the HPC samples, an unusual microcrack pattern is also observed near the rebar-concrete interface (Fig. 9). The microcracks have a random orientation and widths of about 1μm or smaller, and are filled with corrosion products. To our knowledge, these features have not been reported in previous publications. It is not clear how these were formed, but their characteristics suggest a shrinkage-related origin. It is clear from Fig. 9 that the microcracks provide preferential routes for corrosion products to penetrate deeper into the cement paste.

Inner/outer product, rims and relicts of reacted slag

Fig. 10 shows a BSE image and EDX element maps of cement paste between two large aggregate particles near a corroding steel-concrete interface in sample HPC-A-40. A distinct boundary between the corrosion penetration front

and the unaffected paste is visible in the BSE image, Fe, Ca and O maps. The paste area that appears brighter in the BSE image matches very well with the area having higher concentrations of Fe and O, but lower Ca in the EDX maps. Note also the presence of numerous unreacted cement, slag and fly ash particles, as well as relicts of reacted slag particles. Between them are the products of hydration conventionally classified as inner or outer products, defined approximately as those formed in the spaces originally occupied by the clinker and by water respectively [34, 35]. The images show that the corrosion products can be found in the inner as well as the outer products, but not in the dense unreacted cores of the slag, fly ash and cement particles.

Fig. 11 shows a high magnification BSE image and corresponding EDX maps of a boundary between the corrosion-layer and corrosion-filled paste that highlights the hydration rims and relicts of reacted slag particles. A large fly ash particle is present at the lower left corner of the image. The Mg map shows the original boundary of the slag particle since Mg has low solubility and is not expected to migrate in the alkaline pore solution [36]. The Ca map shows the unreacted region of the slag and in this image, all except the largest particle appear to have reacted completely. The reacted rims have widths of several microns, depending on the size of the slag particle and degree of reaction. The rims and relicts are enriched in Mg, Al and Si. Some apparent relicts could be part of larger slag particles that have been sectioned at edges. These features are common and have been studied extensively [33, 37, 38]. However, significant quantities of Fe and O were also detected in the rims and relicts, indicating deposition of corrosion products in the reacted region of the slag particles.

3.4 Quantitative EDX microanalyses

Quantitative X-ray spot analysis was carried out on the corrosion products, C-S-H gel, unreacted slag, and the rims and relicts of reacted slag particles. Results are shown in Table 2. The corrosion products in the macrocracks are composed mainly of Fe (~54% wt.) and O (~29% wt.) with trace quantities of other elements. The corrosion products in the air voids have approximately similar quantities of Fe (~52% wt.) and O (~25% wt.), but significantly higher amounts of Ca (~2% wt) and Na (~1% wt.). The Ca and Na are probably leached from the hydrates and pore solution, which suggests that the corrosion products found in air voids may have penetrated the cement paste through the pores and microcracks.

The corrosion products in macrocracks have a marginally lower mean Fe/O atomic ratios (0.51 ± 0.02) compared to those in air voids (0.57 ± 0.04) and the dark corrosion layer (0.56 ± 0.02). This suggests a slightly increased oxidation level in the cracks due to a greater supply of oxygen. A mean Fe/O atomic close to 0.5 suggests a mixture of oxy hydroxides (FeO(OH)) and ferrous hydroxide ($Fe(OH)_2$), consistent with the expectation that these were formed in an oxygen-rich environment. However, the Fe/O ratios of individual spots vary significantly from 0.3 up to 0.8, which indicates a complex mixture that could include oxides (Fe_3O_4, Fe_2O_3), ferric hydroxide (($Fe(OH)_3$) or hydrated oxides (eg. $Fe(OH)_3.3H_2O$). Note that hydrated oxides cannot be detected using EDX because dehydration would have occurred during sample preparation and imaging. However, its presence may be speculated from the analysis totals (Table 2) that are considerably lower than 100%. It should be noted here that a lot of care was taken during sample preparation to minimise any further oxidation that would have otherwise affected the interpretation of the EDX results. The samples were dried, epoxy-impregnated, polished and analysed immediately after sectioning. In addition, the EDX results were obtained by averaging a large number of analyses and the 95% confidence intervals are small relative to the averages.

The mean atomic ratios of the major elements relative to Ca for the C-S-H gel, unreacted slag, and rims and relicts in the unaffected paste areas are quite similar to values obtained in previous studies [e.g. 28, 34, 35, 36]. The mean Ca/Si ratios for the C-S-H gel in the NC and HPC mix are 1.72 and 1.41 respectively. The lower Ca/Si ratio of the C-S-H gel in the blended concrete compared to the normal concrete is consistent with previous studies [25, 39, 40]. This is due to the pozzolanic reaction of the slag and fly ash, which consumes portlandite to produce C-S-H gel with a lower Ca content. Analysis totals of hydrated cement paste yield values considerably lower than that expected from the content of bound water in the C-S-H gel, and this has been attributed to the presence of porosity in the gel [28, 29, 30]. Nevertheless, the totals for the steel, mill scale, unreacted cement and slag are very close to 100% since these contain very little water or porosity.

In the paste areas affected by corrosion products, the mean atomic ratios of all the major elements relative to Ca for the C-S-H gel, rims and relicts of slag have increased significantly. The Fe/Ca ratio shows the largest increase, by a factor of 80 and 220 for NC and HPC respectively, compared to other ratios that went up by a factor of 5 at most. Thus, the results show that the affected paste is depleted in Ca, but significantly enriched in Fe. The loss of Ca is probably due to leaching of the portlandite and partial decalcification of the C-S-H gel, and seems more severe in the blended concrete (HPC) compared to the normal concrete (NC), despite a lower degree of corrosion in the blended concrete. The analysis totals of the affected paste have also increased significantly compared to the unaffected paste. This confirms that the porosity of the C-S-H gel and rims and relics of reacted slag has decreased due to presence of the corrosion products.

3.5 Extent and distribution of corrosion products penetration

Adjacent BSE images were collected around the steel-concrete interface to produce a montage so that the extent and distribution of the corrosion products penetration can be estimated using image analysis. Nine polished block samples from NC-A, NC-B and HPC-A spanning a range of degrees of corrosion and damage were analysed. Approximately 100 images were required per sample to cover the entire steel-concrete interface at 200x magnification. The coordinates of the images were recorded. For every image and location, the average thickness of the corrosion layer (CL) and the corrosion-penetrated paste (CP) was measured. The areas of the CL and CP of the entire sample were estimated using point-count analysis, and expressed as a percentage of the original rebar cross-sectional area. The lengths of the CL and CP were also measured and expressed as percentages of the rebar perimeter.

Figs. 12 and 13 present the results plotted against degree of corrosion (from 2.4). The results collectively show that as the sample becomes more corroded, the amount of corrosion products that has accumulated at the steel-concrete interface (CL) increases significantly, while the amount that has penetrated the cement paste (CP) stays relatively constant. Similar observations can be made from the measured length and thickness, which increase significantly more for CL compared to CP, as the percentage of corrosion increases. In the most corroded sample, almost 90% of the rebar perimeter is covered by CL. The CP was found to be concentrated near the top of the rebar, which was expected since this is where corrosion initiated due to its proximity to the exposed surface. The length of the CP is typically about 20-25% of the rebar perimeter. Although the local thickness of the CL and CP is highly variable, their averaged values (Fig. 13) display a similar trend to the area and length measurements. The extent of penetration does not appear to increase significantly with the progress of corrosion.

4. Discussion

When steel in concrete corrodes, the oxidation of iron in the anodic region produces soluble ferrous ions (Fe^{2+}), balanced by reduction of oxygen in the cathodic region that forms hydroxyl (OH^-) ions. The presence of chloride ions greatly influences the mechanism and kinetics of the corrosion process. The exact mechanism is believed to involve soluble intermediary 'green complexes' [9]. These ions dissolve in the concrete pore solution, which enables them to move through the pore structure of the cement paste away from the anodic and cathodic regions, probably via a combination of electro-migration and diffusion. These soluble species then undergo further oxidation to form solid precipitates.

The effect of corrosion products penetrating the cement paste is clearly evident from the BSE images, EDX maps and quantitative spot analysis. It is interesting to note that the corrosion products do not penetrate the aggregate-paste ITZ preferentially compared to the bulk paste region. In fact, the transport of corrosion products is hindered by the aggregates, but facilitated by microcracking (e.g. Fig. 9). These observations seem to be in line with our recent study on the influence of ITZ on mass transport properties [41]. Significant quantities of corrosion products were found in the outer and inner hydration products, as well as in rims and relicts of reacted slag particles. This suggests that the transport occurs through capillary pores (empty spaces originally occupied by the mix water). The corrosion products may be oxidised in transit when they enter oxygen-rich areas such as air voids, to form less soluble products.

Another interesting observation is that the paste areas that showed Ca depletion correspond very well with areas affected by corrosion products penetration. This suggests that the two are related. The observed Ca depletion is not surprising since steel corrosion is known to cause acidification near anodic sites from the hydrolysis of ferrous ions [3]. The local fall in pH promotes dissolution of the hydrates, particularly portlandite, to release hydroxyl ions to maintain an alkaline environment [42]. However, the presence of chloride stabilises the local fall of pH by forming hydrochloric acid [43] and amplifies decalcification by forming soluble calcium chloride [44, 45]. The C-S-H gel is less soluble, but can also be decalcified when the portlandite becomes locally depleted. Thus, the blended cement concrete, which has a lower portlandite content, displayed a higher increase in Si/Ca ratio than the normal concrete when decalcified.

The leaching of portlandite followed by progressive decalcification of the C-S-H gel is expected to increase the local porosity and ionic diffusivity [46, 47]. This probably facilitates the transport of soluble corrosion products into the cement paste. However, from the measured increase in analysis totals, the net effect on the pore structure is densification. When the pores become filled or blocked by solid precipitates, the cement paste can no longer accommodate more corrosion products and subsequent products are forced to accumulate at the steel-concrete interface. This produces expansive stresses, which then lead to bond failure between the steel and concrete, and finally through-thickness cracking of the concrete cover.

Our results (Figs 4a, 12 & 13) show that very little build-up of corrosion products is required to cause cover cracking. The exact amount of corrosion products needed to induce the first crack is obviously very difficult to ascertain, but our data suggest an average thickness of about 100 μm with a length that covers approximately 20% of the rebar perimeter. This equates to a local steel radius loss of approximately 25-50 μm, assuming that the specific volume of the corrosion layer (relative to steel) ranges from 2 to 4. However, the critical stress at which cover cracking occurs probably depends on many factors including the mechanical properties of the concrete, cover depth (note that in this work the cover depth was only 20mm), rebar diameter and spacing and proximity to a corner. Clearly, more work is needed to examine the influence of these factors, but our current results seem in line with some previous estimates. For example, Brown [48] suggested that cover cracking occurs when the thickness of the corrosion layer deposited around rebar reaches 0.1-

0.2mm. Andrade et al. [49] and Alonso et al [11] have estimated that a steel radius loss of about 15-50 μm is needed to generate the first visible crack (<0.1 mm) for concretes with a w/c ratio range of 0.50-0.65 and cover/rebar diameter ratio range of 1-7. However, these estimations are for uniform corrosion accelerated by applied current and are based on conversion from corrosion rate using Faraday's law, which assumes 100% current efficiency. No direct measurements of the actual corrosion products thickness and distribution were made.

The bond failure and full-depth cover cracks will increase the supply of moisture, oxygen and chloride to the steel and accelerate the corrosion process. The most hydrated and oxygen-rich corrosion products will form in the cracks that are accessible to the external environment. It is noted that while some cracks are partially filled with corrosion products, others remain virtually empty. This suggests that crack growth and propagation is not caused by infilling of the cracks with corrosion products. However, the cracks offer a preferred route for the corrosion products to be transported away from the corrosion sites. Thus, as the sample becomes more corroded, the extent of penetration into the cement paste stays relatively unchanged, at approximately 100-200 μm and covers about 20% of the rebar perimeter (Fig. 12 & 13). It is likely that the volume of paste that can accommodate corrosion products during the 'free-expansion' period is no larger than this value.

It is important to relate the findings of this study to the way in which time to cover cracking due to rebar corrosion is currently modelled. Our results support the assumption of a 'porous zone' that can accommodate corrosion products, prior to stress development. However, our measurements found penetration depths significantly greater than the 12.5 μm specified by Liu & Weyers [12]. In addition, our results show that the corrosion products fill not only the capillary pores and air voids, but also pores inherent in the hydrates or created by dissolution of the hydrates. This is yet to be considered in available models. Current models, based on the idealisation of concrete cover as a thick-walled hollow cylinder, also assume a uniform loss of steel cross-sectional area around the rebar, but this is seldom the case because corrosion tends to be unevenly distributed with the most severely corroded areas being closest to the exposed concrete surface. Indeed, our study found that the 'porous zone' covers only a fraction of the rebar perimeter, the extent of which will probably depend on the exposure environment and sample geometry. In practice, the geometrical characteristics of cover cracking are a function of the location and spacing of the rebar so models that consider a single rebar in isolation may be an oversimplification. The beneficial effect of transverse reinforcement, such as shear links, in mitigating cover cracking also needs to be considered. Hence, due to the reasons above, it would not be meaningful to apply our values to existing models for predicting time to cracking. Clearly, more detailed experimentation coupled with model development is necessary.

Like any empirical study, the results and conclusions from this work are only strictly valid for the samples investigated and so caution must be exercised if one wishes to extend these findings to other situations. More work needs to be done for example, to study the effect of exposure environment and corrosion rate, which are likely to influence the amount of corrosion products that can be accommodated prior to cracking. For example, it is known that extensive corrosion can occur in situations of low oxygen availability without forming expansive solid products that cause cracking. When the anodic sites are starved of oxygen, such as in samples submerged in water for extended periods, the corrosion products can remain in solution and travel through the cover without any visible deterioration to the sample. This type of corrosion is known as 'black' or 'green' corrosion due to the colour of the rust liquid when first exposed to air [2, 5, 9]. Corrosion under anoxic condition needs to be considered separately. The detailed mechanism and associated kinetics with respect to the transport of soluble corrosion products and their binding to cement hydrates are also complex and require further study.

5. Conclusions

Corrosion of steel in reinforced concrete produces soluble corrosion products that can migrate or diffuse through the cement paste. This study observed that the corrosion products can be deposited in air voids, in the outer and inner hydration products and in rims and relicts of reacted slag. A distinct boundary between the affected and unaffected paste areas can be seen in BSE images, indicating the extent of the penetration front. The corrosion products penetrates the aggregate-paste ITZ as well as the 'bulk' paste farther away. The affected paste areas have higher analysis totals, and Fe and O contents, but are depleted in Ca. The latter indicates that dissolution of portlandite and partial decalcification of the C-S-H gel have occurred. This increases the local porosity and diffusivity, which then facilitate corrosion product transport. Thus, the corrosion products fill not only the capillary pores and air voids, but also pores inherent in the hydrates and created by dissolution of the hydrates. However, when the pores become filled or blocked by solid corrosion products, subsequent products are forced to accumulate at the steel-concrete interface, inducing expansive pressure that leads to bond failure and cracking of the concrete cover. Our results suggest that only a small amount of corrosion product, approximately 100 μm thick covering about 20% of the rebar perimeter, is needed to generate the first visible cover crack (~0.05 mm width). Once cracking has initiated, the corrosion products is preferentially deposited in the large cracks rather than pore spaces in the cement paste. Hence, the extent of corrosion products penetration does not increase much with corrosion. It is estimated that the amount of cement paste that can accommodate corrosion products during the 'free-expansion' stage, for the samples investigated, is no more than 100 μm thick covering about 20% of the rebar perimeter. However, further investigations are required to examine the influence of other variables, including exposure conditions and corrosion rate.

Acknowledgements

HSW acknowledges the financial support provided by the Engineering and Physical Sciences Research Council, UK. YXZ would like to thank the National Natural Science Foundation of China (Grant number 50538070 & 50808157) for supporting her academic visit to Imperial College. We wish to express our thanks to Mr. Andrew Morris for his help in preparing the samples for microscopy work.

References

[1] D. Talbot, J. Talbot, Corrosion Science and Technology, CRC Press, London, 1998.

[2] A. Bentur, S. Diamond, N.S. Berke, Steel Corrosion in Concrete. Fundamentals and Civil Engineering Practice, Taylor & Francis, 1997.

[3] L. Bertolini, B. Elsener, P. Pedeferri, R. Polder, Corrosion of Steel in Concrete, Wiley, 2004.

[4] ACI Committee 222, Protection of metals in concrete against corrosion, ACI 222R-01, ACI Manual of Concrete Practice, 2005.

[5] J.P. Broomfield, Corrosion of steel in concrete, understanding, investigation and repair, 2nd Edition, Taylor & Francis, London, 2007.

[6] K.K. Sagoe-Crentsil, F.P. Glasser, Steel in concrete: Part I A review of the electrochemical and thermodynamic aspects, Mag. Concr. Res., 41 (1989) 205-212.

[7] F.P. Glasser, K.K. Sagoe-Crentsil, Steel in concrete: Part II Electron microscopy analysis, Mag. Concr. Res., 41 (1989) 213-220.

[8] RT Foley, Role of chloride ion in iron corrosion, Corrosion, 26 (1970) 58-70.

[9] K.K. Sagoe-Crentsil, F.P. Glasser, 'Green corrosion products', iron solubility and the role of chloride in the corrosion of steel at high pH, Cem. Concr. Res. (1993) 23, 785-791

[10] M.L. Allan, Probability of corrosion induced cracking in reinforced concrete, Cem. Concr. Res., 25 (1995) 1179-1190.

[11] C. Alonso, C. Andrade, J. Rodriguez, J.M. Diez, Factors controlling cracking of concrete affected by reinforcement corrosion, Mater. Struct., 31 (1998) 435-441.

[12] Y.P. Liu, R.E. Weyers, Modeling the time-to-corrosion cracking in chloride contaminated reinforced concrete structures, ACI Mat J, 95 (1998) 675-681.

[13] K. Bhargava, A.K. Ghosh, Y. Mori, S. Ramanujam, Modeling of time to corrosion-induced cover cracking in reinforced concrete structures, Cem. Concr. Res., 35 (2005) 2203-2218.

[14] D. Chen, S. Mahadevan, Chloride-induced reinforcement corrosion and concrete cracking simulation, Cem. Concr. Comp., 30 (2008) 227-238.

[15] I. Petre-Lazar, B. Gérard, Mechanical behaviour of corrosion products formed at the steel-concrete interface. Testing and Modelling, EM2000 Proc. 14th Engineering Mechanics Conference, ASCE, Austin, Texas, 2000.

[16] K. Suda, S. Misra, K. Motohashi, Corrosion products of reinforcing bars embedded in concrete, Corrosion Science, 35 (1993) 1543-1549.

[17] A.G. Constantinou, K.L. Scrivener, Microstructural examination of the development of corrosion in reinforced concrete, In: Mechanisms of chemical degradation of cement-based systems, in: K.L. Scrivener, J.F. Young (Eds.), E & FN Spon, London, 1995, 134-142.

[18] A.K. Aligizaki, M.R. de Rooij, D.D. Macdonald, Analysis of iron oxides accumulating at the interface between aggregates and cement paste, Cem. Concr. Res., 30 (2000) 1941-1945.

[19] G.S. Duffó, W. Morris, I. Raspini, C. Saragovi, A study of steel rebars embedded in concrete during 65 years, Corros. Sci., 46 (2004) 2143-2157.

[20] O. Poupard, V.L'Hostis, S. Catinaud, I. Petre-Lazar, Corrosion damage prognosis of a reinforced concrete beam after 40 years natural exposure in marine environment, Cem. Concr. Res., 36 (2006) 504-520.

[21] T.D. Marcotte, C.M. Hansson, Corrosion products that form on steel within cement paste, Mater Struct., 40 (2007) 325-340.

[22] S. Caré, Q.T. Nguyen, V. L'Hostis, Y. Berthaud, Mechanical properties of the rust layer induced by impressed current method in reinforced mortar, Cem. Concr. Res., 38 (2008) 1079-1091.

[23] W-J Chitty, P. Dillmann, V. L'Hostis, C. Lombard, Long-term corrosion resistance of metallic reinforcements in concrete—a study of corrosion mechanisms based on archaeological artefacts, Corros. Sci., 47 (2005) 1555-1581.

[24] V. L'Hostis, F. Foct, P. Dillmann, Corrosion behaviour of reinforced concrete: Laboratory experiments and archaeological analogues for long-term predictive modeling, Journal of Nuclear Materials, 379 (2008) 124-132.

[25] A.M. Harrisson, N.B. Winter, H.F.W. Taylor, An examination of some pure and composite cement pastes using scanning electron microscopy with X-ray analytical capability, 8th International Congress on the Chemistry of Cement, Rio De Janeiro, 1986, 170-175

[26] H.S. Wong, N.R. Buenfeld, Monte Carlo simulation of electron-solid interactions in cement-based materials, Cem. Concr. Res., 36 (2006) 1076-1082.

[27] J. Pouchou, F. Pichoir, Electron Probe Quantitation, Plenum Press, New York, 1991.

[28] A.M. Harrisson, N.B. Winter, H.F.W. Taylor, X-ray microanalysis of microporous materials, J. Mater. Sci. Lett., 6 (1987) 1339-1340.

[29] K.O. Kjellsen, E.H. Atlassi, X-ray microanalysis of hydrated cement: Is the analysis total related to porosity? Cem. Concr. Res., 28 (1998) 161-165.

[30] C. Famy, K.L. Scrivener, A.K. Crumbie, What causes differences of C-S-H gel grey levels in backscattered electron images? Cem. Concr. Res., 32 (2002) 1465-1471.

[31] D.C. Cook, Spectroscopic identification of protective and non-protective corrosion coatings on steel structures in marine environments, Corros. Sci., 47 (2005) 2250-2570.

[32] W-J. Chitty, P. Berger, P. Dillmann, V. L'Hostis, Long-term corrosion of rebars embedded in aerial and hydraulic binders – Mechanisms and crucial physico chemical parameters, Corros. Sci., 50 (2008) 2117-2123.

[33] J.L. Gallias, Microstructure of the interfacial transition zone around corroded reinforcement, in: A. Katz, A. Bentur, M. Alexander, G. Arliquie (Eds.), The Interfacial Transition Zone in Cementitious Composites, E&FN Spon, London, 1998, 171-178

[34] I.G. Richardson, The nature of C-S-H in hardened cements, Cem. Concr. Res., 29 (1999) 1131-1147

[35] C. Famy, A.R. Brough, H.F.W. Taylor, The C-S-H gel of Portland cement mortars: Part 1. The interpretation of nergy-dispersive X-ray microanalysis from scanning electron microscopy, with some observations on C-S-H, AFm and Aft phase compositions, Cem. Concr. Res., 33 (2003) 1389-1398.

[36] H.F.W. Taylor, D.E. Newbury, An electron microprobe study of a mature cement paste, Cem. Concr. Res., 14 (1984) 565-573.

[37] A.M. Harrisson, N.B. Winter, H.F.W. Taylor, Microstructure and microchemistry of slag cement pastes, Mat. Res. Soc. Symp. Proc., 85 (1987) 213-222

[38] A.P. Barker, An electron optical examination of zoning in blastfurnace slag hydrates: Part 1. Slag cement pastes at early ages, Adv. Cem. Res., 2 (1989) 171-179.

[39] H.F.W. Taylor, K. Mohan, G.K. Moir, Analytical study of pure and extended Portland cement pastes: II Fly ash- and slag-cement pastes, J. Am. Ceram. Soc., 68 (1985) 685-690.

[40] J.I. Escalante-Garcia, J.H. Sharp, The chemical composition and microstructure of hydration products in blended cements, Cem. Concr. Comp., 26 (2004) 967-976.

[41] H.S. Wong, M. Zobel, N.R. Buenfeld, R.W. Zimmerman, Influence of the interfacial transition zone and microcracking on the diffusivity, permeability and sorptivity of cement-based materials after drying, Mag. Concr. Res., 61 (2009) 571-589.

[42] G.K. Glass, B. Reddy, N.R. Buenfeld, Corrosion inhibition in concrete arising from its acid neutralisation capacity, Corros. Sci., 42 (2000) 1587-1598.

[43] G.K. Glass, B. Reddy, N.R. Buenfeld, The participation of bound chloride in passive film breakdown on steel in concrete, Corros. Sci., 42 (2000) 2013-2021.

[44] P. Gégout, E. Revertégat, G. Moine, Action of chloride ions on hydrated cement pastes: Influence of the cement type and long time effect of the concentration of chlorides, Cem. Concr. Res., 22 (1992) 451-457.

[45] A. Delagrave, M. Pigeon, J. Marchand, E. Revertegat, Influence of chloride ions and pH level on the durability of high performance cement pastes (Part II), Cem. Concr. Res., 26 (1996) 749-760.

[46] E. Revertégat, C. Richet, P. Gégout, Effect of pH on the durability of cement pastes, Cem. Concr. Res., 22 (1992) 259-272.

[47] D.P. Bentz, E.J. Garboczi, Modelling the leaching of calcium hydroxide from cement paste: effect on pore space percolation and diffusivity, Mater. Struct., 25 (1992) 523-533.

[48] R.D. Browne, Mechanism of corrosion of steel in concrete in relation to design, inspection, and repair of offshore and coastal structures, In: V.M. Malhotra (Ed.), Performance of Concrete in Marine Environments, ACI SP-65, 1980, 169-204

[49] C. Andrade, C. Alonso, F.J. Molina, Cover cracking as a function of bar corrosion: Pt 1. Experimental test, Mater. Struct. 26 (1993) 453-464.

Tables

Table 1 Mixture proportions

Mix	Water/binder ratio	Binder (kg/m^3)			Aggregate (kg/m^3)		Admixture (l/m^3)	
		Cement	Slag	Fly ash	Gravel	Sand	Superplasticiser	Corrosion inhibitor
NC	0.44	439	-	-	1161	571	-	-
HPC	0.345	126	168	126	1068	735	5.0	8.4

Table 2 Results from quantitative EDX microanalysis

	n	Mean atomic ratios relative to Ca					Fe/O	Analysis totals (%)
		Mg	Al	Si	S	Fe		
Uncorroded steel	94	-	-	-	-	-	38.8 ± 2.2	100.7 ± 0.8
Millscale	129	-	-	-	-	-	0.91 ± 0.04	100.9 ± 2.0
Corrosion products in:								

i. Corrosion-layer (lighter)	188	-	-	-	-	-	0.84 ± 0.08	93.2 ± 0.8
ii. Corrosion-layer (darker)	223	-	-	-	-	-	0.56 ± 0.02	88.8 ± 0.8
iii. Cracks	138	-	-	-	-	-	0.51 ± 0.02	93.6 ± 1.6
iv. Air voids	116	-	-	-	-	-	0.57 ± 0.04	88.9 ± 1.2
C-S-H gel:								
i. NC	176	0.03 ± 0.004	0.08 ± 0.01	0.58 ± 0.02	0.03 ± 0.004	0.04 ± 0.01	0.02 ± 0.004	56.6 ± 1.4
ii. NC*	314	0.05 ± 0.01	0.12 ± 0.01	0.65 ± 0.04	0.03 ± 0.004	3.27 ± 0.26	0.47 ± 0.02	74.6 ± 0.6
iii. HPC	112	0.04 ± 0.006	0.27 ± 0.06	0.71 ± 0.06	0.03 ± 0.006	0.03 ± 0.004	0.01 ± 0.002	63.8 ± 1.4
iv. HPC*	153	0.20 ± 0.05	0.73 ± 0.08	2.73 ± 0.31	0.03 ± 0.003	6.65 ± 0.78	0.41 ± 0.02	77.1 ± 0.8
Slag:								
i. Unreacted	64	0.26 ± 0.01	0.40 ± 0.02	0.82 ± 0.04	0.04 ± 0.004	0.02 ± 0.004	0.01 ± 0.004	94.0 ± 0.4
ii. Rims and relicts	75	0.43 ± 0.04	0.35 ± 0.04	0.73 ± 0.04	0.05 ± 0.01	0.02 ± 0.002	0.01 ± 0.002	60.4 ± 1.8
iii. Rims and relicts*	85	0.93 ± 0.20	0.71 ± 0.22	1.61 ± 0.2	0.03 ± 0.004	4.87 ± 1.54	0.35 ± 0.04	73.9 ± 1.8

Notes: n = number of analyses. Results are presented as mean ± 95% confidence interval ($2\sigma/\sqrt{n}$). Superscripts * represent analyses obtained from the 'corrosion-filled paste' (CP) areas.

Figures

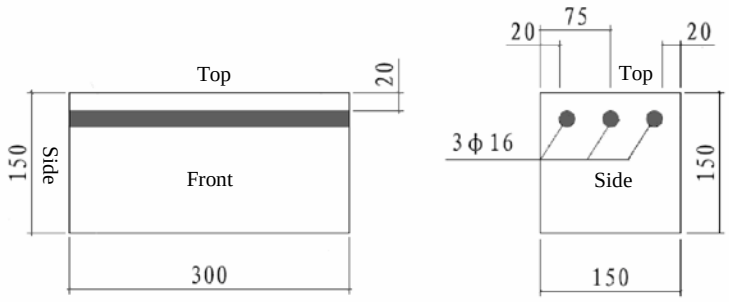

Figure 1 Schematic of the reinforced concrete panel showing the rebar arrangement (dimensions are in mm)

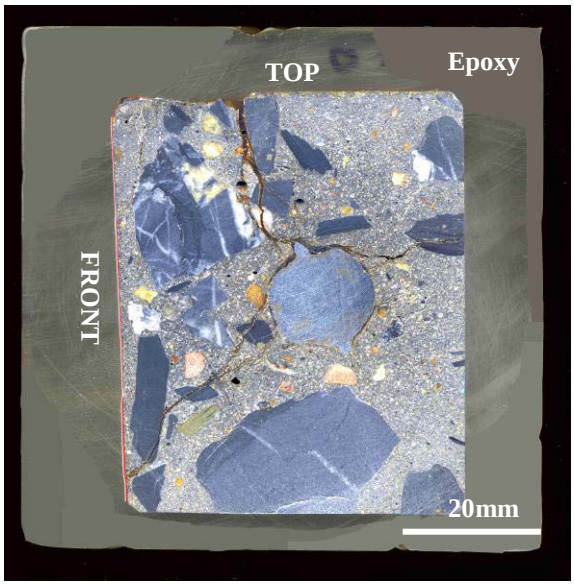

Figure 2 Image of an 8 mm thick slice obtained using a flatbed scanner at 1200 dpi

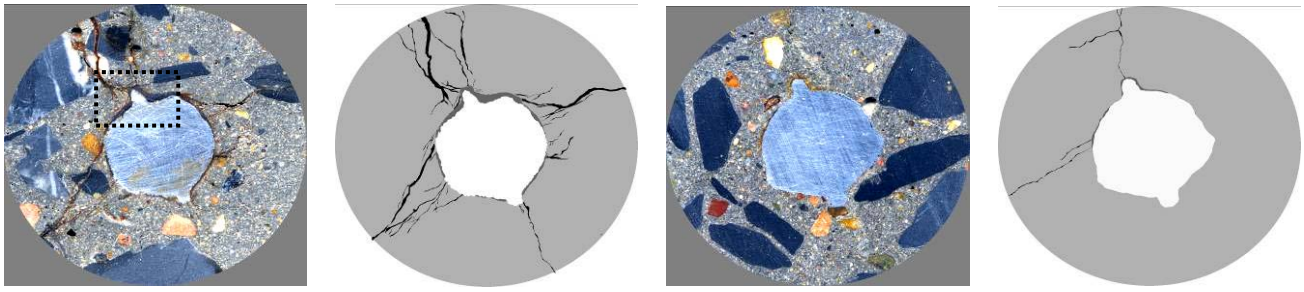

a) NC-A-10 mm, Corrosion = 8.47%, Damage = 13.8%

b) NC-A-80 mm, Corrosion = 0.72%, Damage = 1.0%

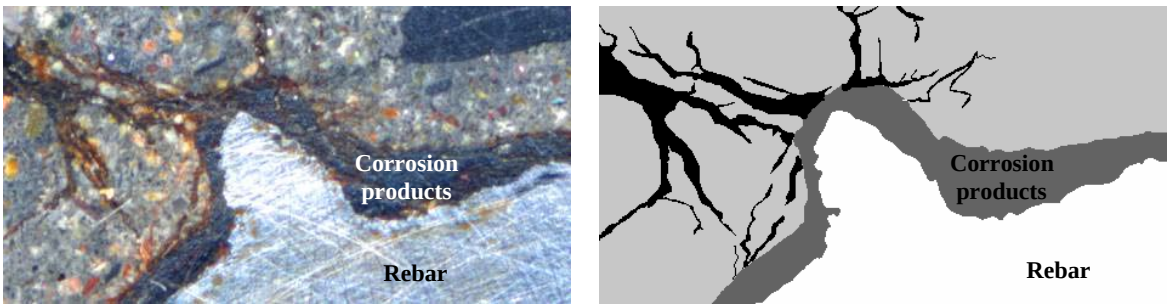

c) Magnified portion of the boxed area in figure (a)

Figure 3 Two examples of original and segmented images used for measuring the area fraction of cracks and corrosion products at the rebar-concrete interface

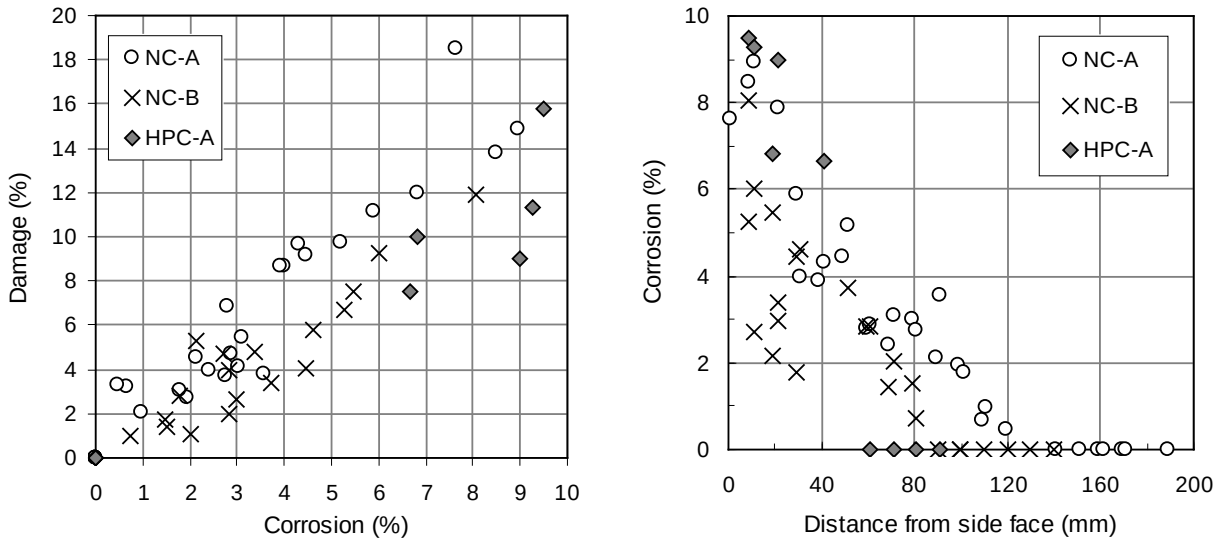

(a) (b)

Figure 4 a) Correlation between the amount of corrosion and damage measured on each slice, and b) variation in the amount of corrosion along the length of each panel.

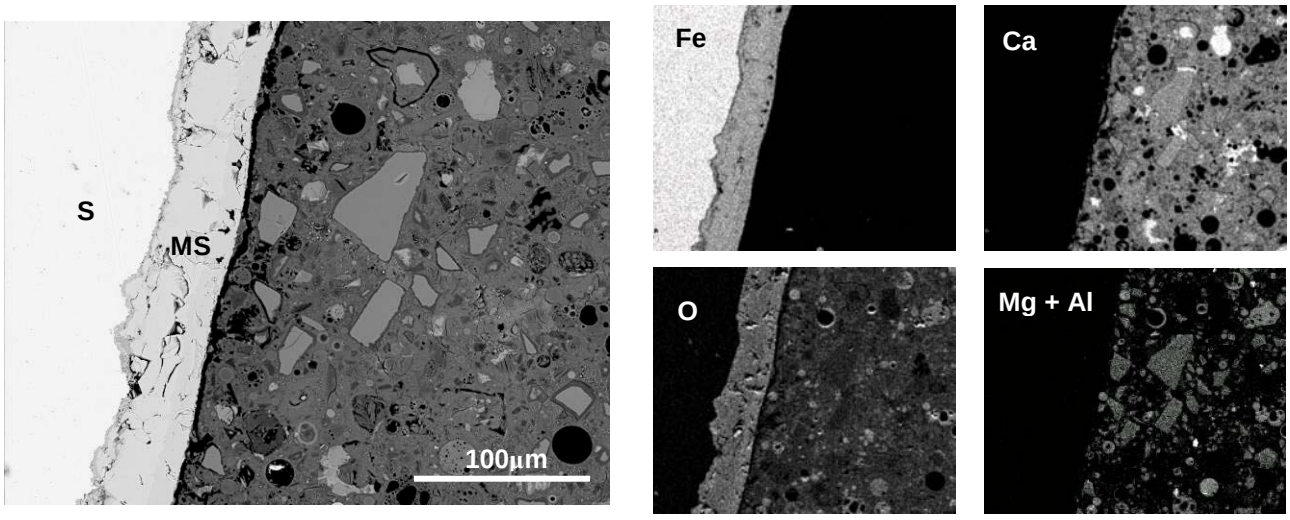

(a) (b)

Figure 5 a) BSE image and b) EDX element maps of a steel-concrete interface not affected by corrosion. (S: Steel; MS: Millscale; field of view: 343x 274µm, sample is HPC-A-60)

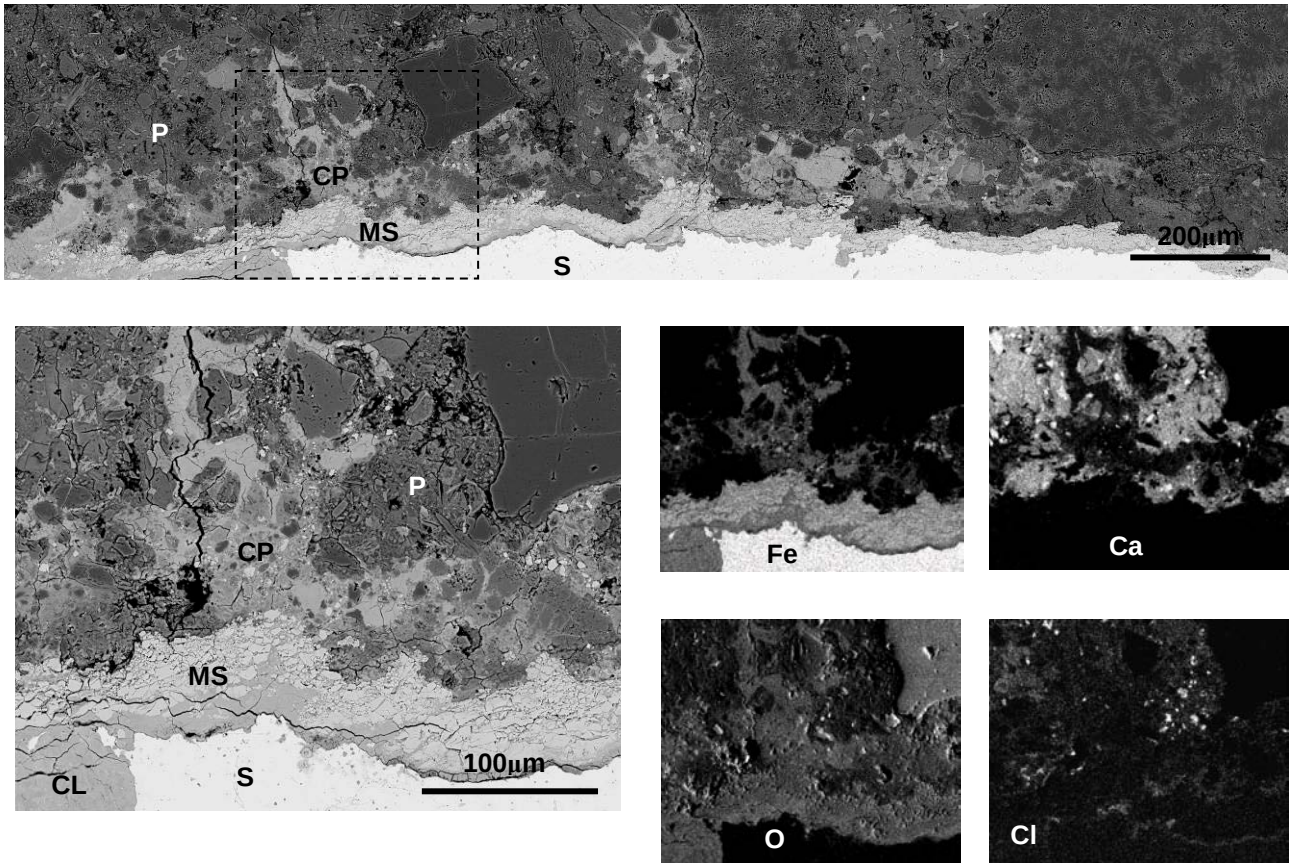

Figure 6 BSE montage from NC-A-110 showing mild corrosion (0.98%) and corrosion products penetrating the cement paste matrix. EDX element maps of the boxed area indicate the original boundary of the rebar-concrete interface, extent of penetration and decalcification. (S: Steel; MS: Millscale; CL: Corrosion layer; CP: Corrosion-filled paste; P: Unaltered paste)

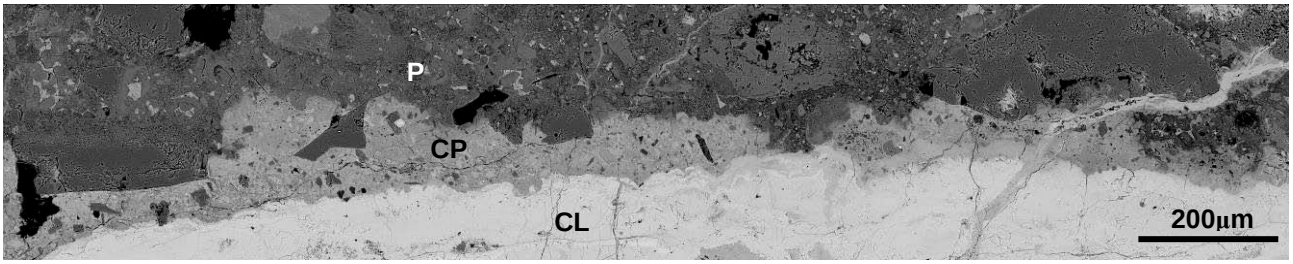

(a) NC-A-20 (Field of view: 1837 x 363 µm)

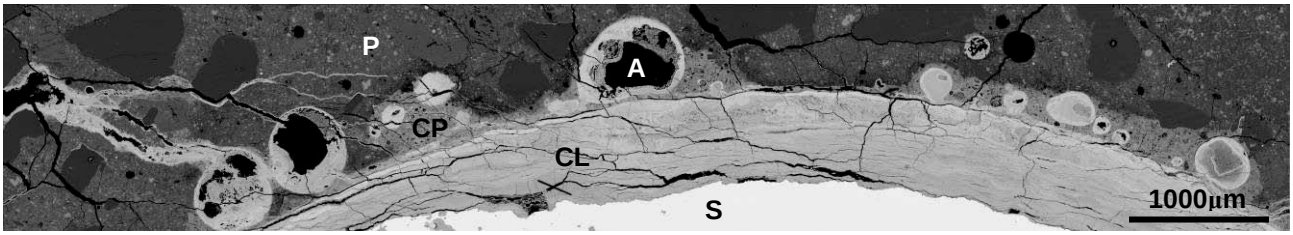

(b) HPC-A-40 (Field of view: 9567 x 1687 µm)

Figure 7 BSE montage images taken from NC-A-20 (6.81% corrosion) and HPC-A-40 (6.65% corrosion) showing accumulation of corrosion products at the steel-concrete interface and migration of corrosion products into the cement paste, air voids and cracks. (S: Steel; CL: Corrosion layer; CP: Corrosion-filled paste, P: Unaltered paste; A: Air voids)

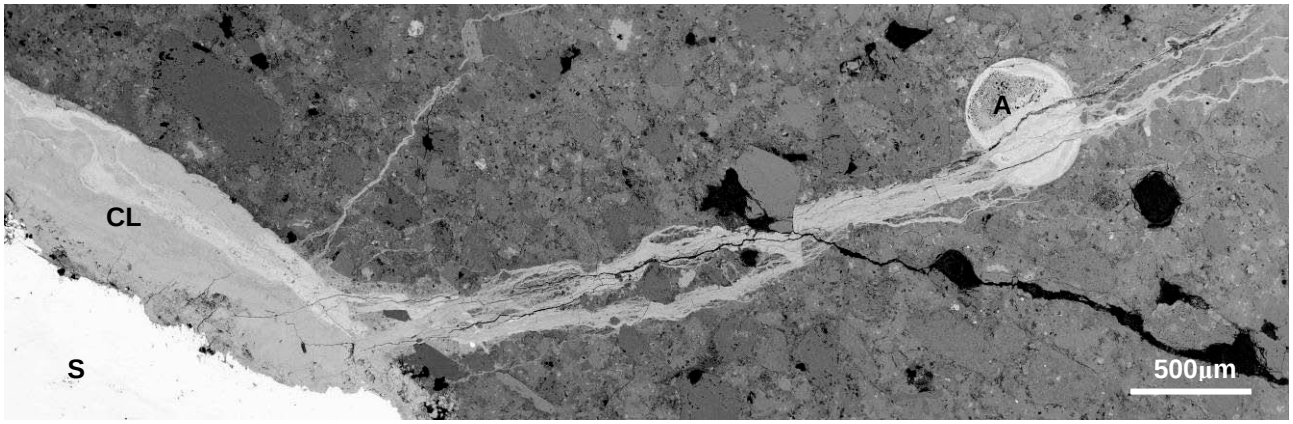

Figure 8 BSE montage from NC-A-40 (4.29% corrosion) that shows a large crack propagating from the steel-concrete interface where a thick layer of corrosion products has accumulated. No significant penetration of corrosion products into the cement paste is visible here. (Field of view: 5363 x 1725 µm)

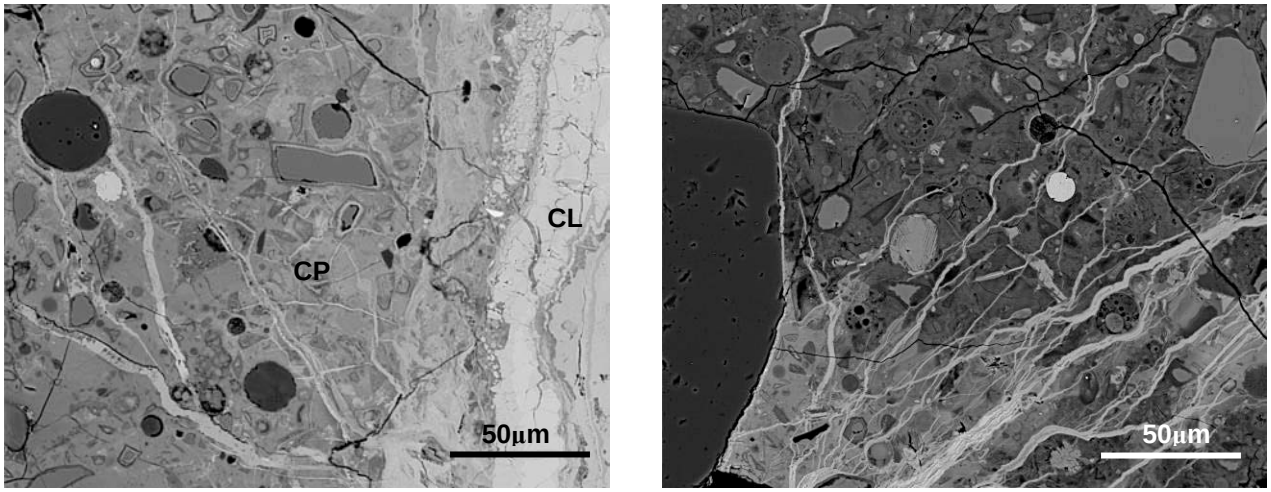

Figure 9 Fine microcracks detected on HPC-A-40 (6.65% corrosion) near the concrete-rebar interface. (Field of view: 218 x 175 µm)

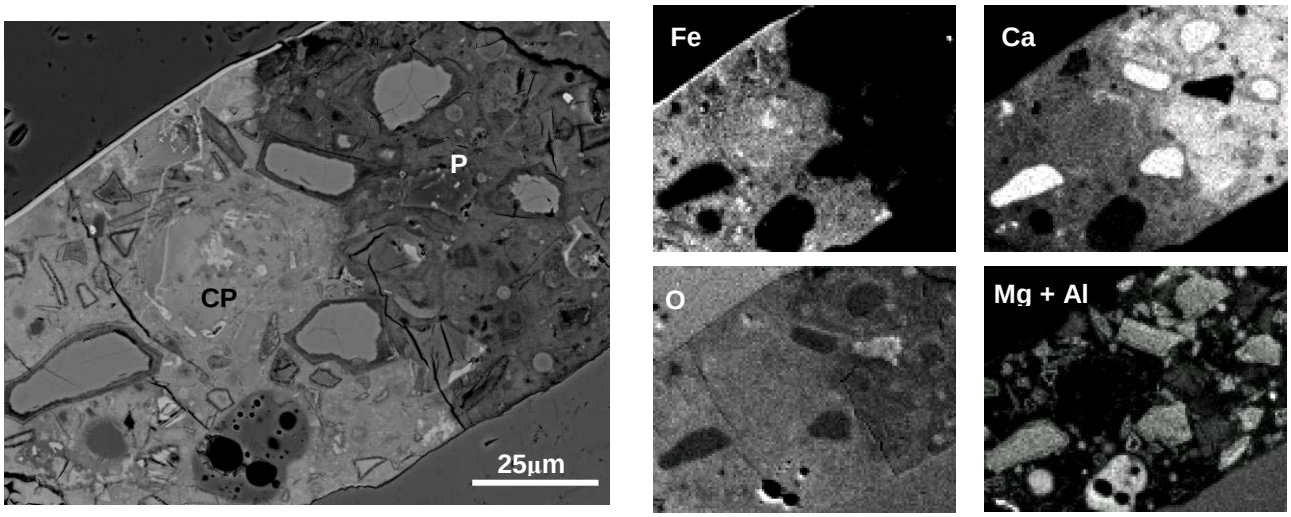

Figure 10 BSE image and EDX element maps of cement paste between two large aggregates highlighting the distinct boundary and area where corrosion products have penetrated. The corrosion products appear to have migrated through pore spaces in the inner as well as outer hydration products. (Sample is HPC-A-40. Field of view: 120 x 96 µm)

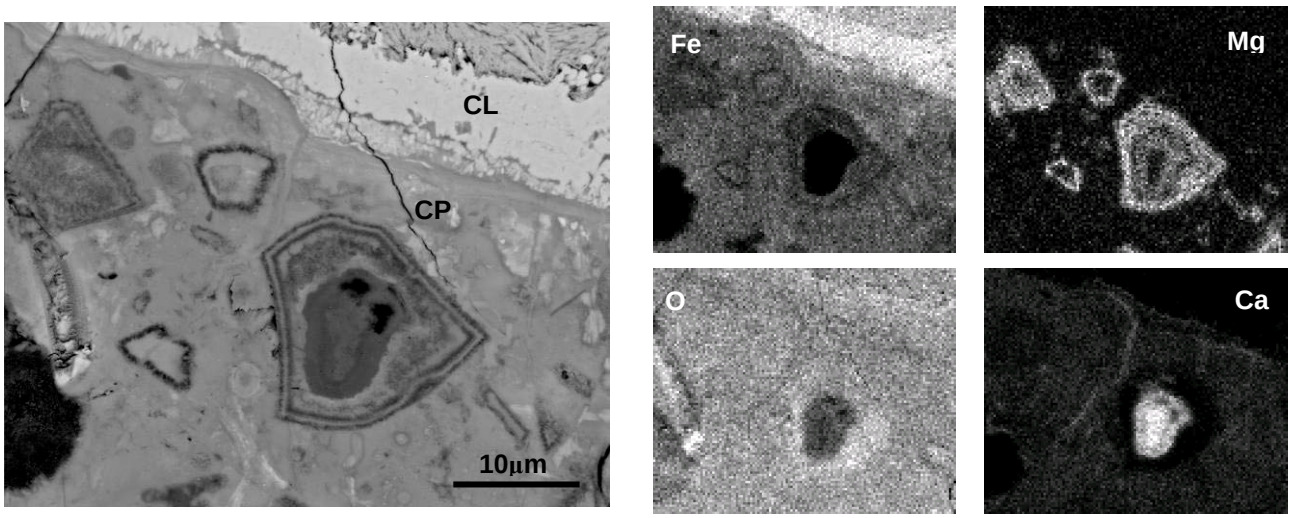

Figure 11 BSE image and EDX element maps of a boundary between the corrosion-layer (CL) and corrosion-filled paste (CP). The corrosion products appear to have migrated through the outer rim into the region of low Ca within the slag particle where it has reacted. (Sample is HPC-A-40. Field of view: 48 x 24 µm)

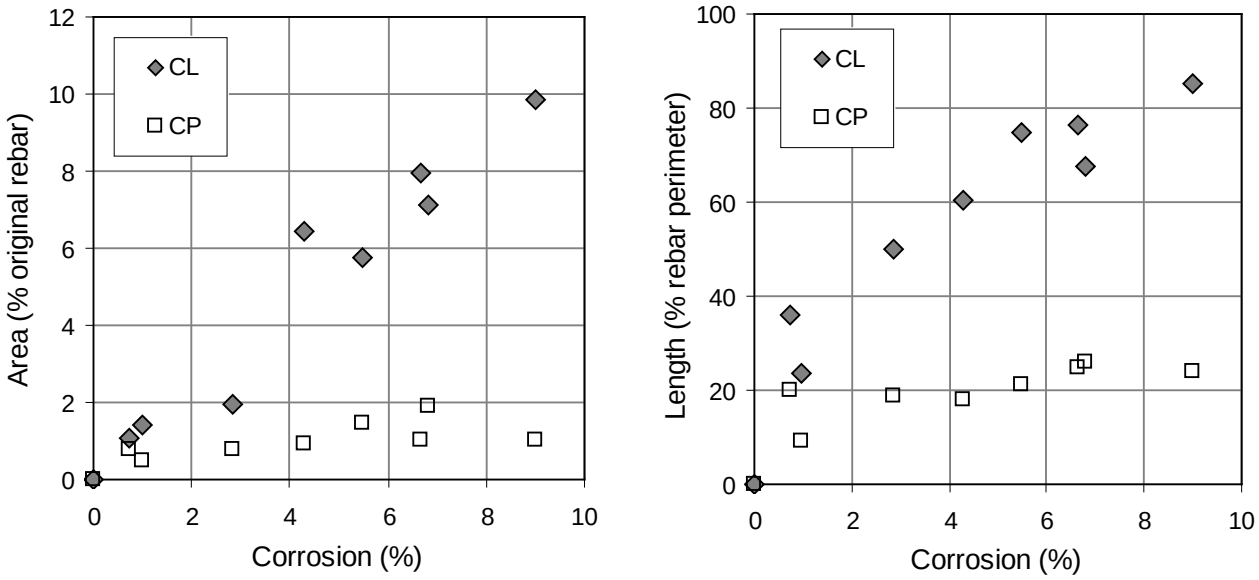

Figure 12 Area and length of the corrosion layer (CL) and corrosion penetrated paste (CP) plotted against amount of corrosion.

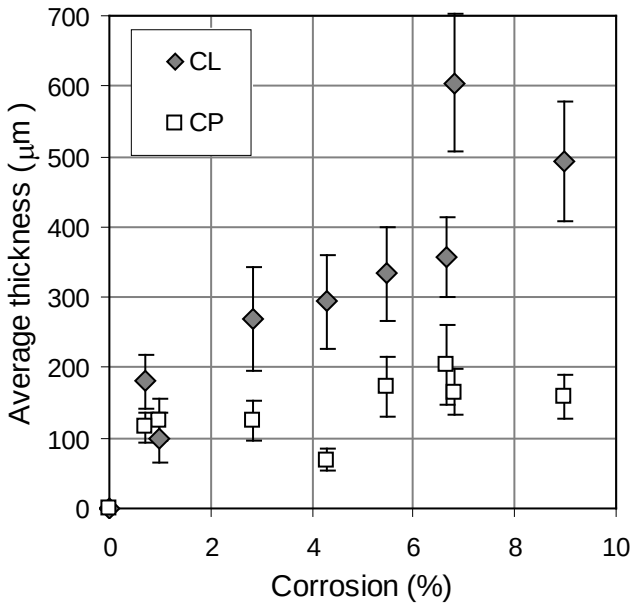

Figure 13 Average thickness of the corrosion layer (CL) and corrosion-penetrated paste (CP) plotted against amount of corrosion. Error bars indicate ± 95% confidence interval.